Check for updates

Research Article

Advances in Mechanical Engineering

Advances in Mechanical Engineering
2018, Vol. 10(7) 1–9
© The Author(s) 2018
DOI: 10.1177/1687814018789800
journals.sagepub.com/home/ade
SAGE

An investigation on kinematics and dynamics performance of a novel 3-PRC-compliant parallel micromanipulator

Xiang-Chun Li[1], Yangmin Li[1,2], Bing-Xiao Ding[3] and Hong-Ye Xu[1]

Abstract

This article proposes a 3-PRC compliant parallel micromanipulator with 3 degrees of freedom. The piezoelectric actuator is adopted to drive the mechanism, and to compensate the stroke of the piezoelectric actuator, a new type of secondary lever amplification mechanism is designed. The kinematics model of the 3-PRC parallel micromanipulation platform is derived using vector method, and the forward and inverse kinematics solutions of a 3-PRC parallel micromanipulation stage are emphatically analyzed and then the Jacobian matrix of kinematics model and workspace are derived. Finally, the dynamic model is established by Lagrange equation, and the natural frequency of the mechanism is calculated. The modal analysis is carried out using finite element method. The results showed that the mechanism has a favorable performance on kinematics and dynamics, and this micromanipulator can achieve micro/nano level motion with high accuracy.

Keywords

3-PRC, secondary lever amplifier, kinematics, dynamics

Date received: 15 July 2017; accepted: 20 June 2018

Handling Editor: Mario L Ferrari

Introduction

With the development of micro/nano technology and robot technology, micromanipulation technology is becoming a hot spot that involves multi-disciplinary fields such as scanning probe microscopy (SPM), lithography, nano-manipulation and manufacturing, and biological science.[1] How to design a novel micromanipulator with compact size, larger stroke, higher precision, higher flexibility, and easier miniaturization is the key part of micromanipulation technology.[2] The compliant mechanism can realize the motion, force and energy transfer, and conversion mainly through the deformation of the flexible elements, while the traditional rigid components realize the specific movement and function through the connection of the motion pair and other components.[3] Compliant mechanisms have been widely used for fiber alignment, atomic force microscopy, and non-circular operation, which possess many advantages: excellent performance (such as high

[1]Tianjin Key Laboratory for Advanced Mechatronic System Design and Intelligent Control, Tianjin University of Technology, Tianjin, China
[2]Faculty of Engineering, Department of Industrial and Systems Engineering, The Hong Kong Polytechnic University, Kowloon, Hong Kong
[3]Department of Electromechanical Engineering, University of Macau, Macau, China

Corresponding author:
Yangmin Li, Faculty of Engineering, Department of Industrial and Systems Engineering, The Hong Kong Polytechnic University, Hung Hom, Kowloon 999077, Hong Kong.
Email: yangmin.li@polyu.edu.hk; yangmin_li@hotmail.com

Creative Commons CC BY: This article is distributed under the terms of the Creative Commons Attribution 4.0 License (http://www.creativecommons.org/licenses/by/4.0/) which permits any use, reproduction and distribution of the work without further permission provided the original work is attributed as specified on the SAGE and Open Access pages (https://us.sagepub.com/en-us/nam/open-access-at-sage).

precision, light weight, and small friction), low cost (such as easy processing and less components), and easy miniaturization (such as micro/nano mechanical devices).[4–7] The piezoelectric actuator is widely adopted to drive the micromanipulator, and to compensate the limited stroke of piezoelectric actuator, the amplifier mechanisms are adopted to meet the large stroke requirements.[8,9] Utilizing an amplifier mechanism is the most effective way to amplify the stroke of micromanipulation stage, and the lever amplifier mechanism, bridge-type amplification mechanism, and Scott-Russell mechanism are commonly used in micromanipulation stages.[10–12]

In the study by Ding et al.,[13] a 3-degree-of-freedom (DOF) planar micromanipulation stage with large rotational displacement for micromanipulation is designed with the workspace of 84.62 μm × 97.12 μm × 10.28 mrad, and the lever mechanism is adopted to magnify the stroke of the piezoelectric actuators in order to get a large workspace. Liu et al.[14] presented an XY parallel nanopositioner with symmetric and two-stage displacement amplifiers, and this mechanism has a large workspace more than 200 μm and a high natural frequency at about 760 Hz. In the study by Li and Xu,[15,16] an XY totally decoupled parallel micromanipulator is presented based on flexure hinges, the bridge-type displacement amplifier is utilized for this stage to amplify the stroke of piezoelectric actuator, and the amplification ratio of bridge-type amplifier is approximately 6. M Muraoka and S Sanada[17] proposed a displacement amplifier for piezoelectric actuator based on honeycomb link mechanism, the maximum displacement of 400 μm along each X axis and Y axis, maximum resolution of 5 nm, and the natural frequency measured approximately 60 Hz. Yong et al.[18] designed a flexure-based XY Stage for fast nanoscale positioning; this stage uses a lever magnifying mechanism to amplify the output displacement of the piezoelectric stack and utilize the parallel quadrilateral mechanism to make the X axis and Y axis decoupled, and the natural frequency of the platform can reach up to 2.7 kHz. U Bhagat et al.[19] proposed a parallel piezoelectric platform based on right circular flexure hinge, which is capable of performing planar motion with 3 DOFs in X axis, Y axis, and θ, which is about 142 mm × 110 mm in size and the workspace is 39.0 μm × 25.0 μm × 0.9 mrad.

This article proposes a compliant parallel micromanipulator based on translational 3-prismatic-revolute-cylindrical (3-PRC) parallel mechanism that can realize three translational motion in space. The novelty of this mechanism employs flexure-based joints for the purposes of avoiding assembly errors and employs secondary lever amplifier to compensate the stroke of the piezoelectric actuator. By the way, the proposed 3-PRC mechanism has the benefit of compactness size, large amplification ratio, and good decoupling characteristic compared with the previous 3-PRC mechanism.[20,21] The remainder of this article is organized as follows: a novel 3-PRC-compliant parallel micromanipulator is proposed in section "3-PRC-compliant parallel micromanipulator design"; the structure of secondary lever amplifier is introduced in detail, the amplification ratio is calculated by lever principle and the results of simulation by ANSYS software is used to verify the theoretical calculation in section "The secondary lever amplifier design"; the kinematic analysis of this manipulation stage is conducted in section "Kinematics model of the 3-PRC-compliant parallel micromanipulator"; in section "Dynamics model of the 3-PRC-compliant parallel micromanipulator," the dynamic characteristics and performance of this stage are evaluated. Finally, the conclusions are concluded in section "Conclusion."

3-PRC-compliant parallel micromanipulator design

As shown in Figure 1(a), the micromanipulator is composed of a fixed base, a mobile platform, and three

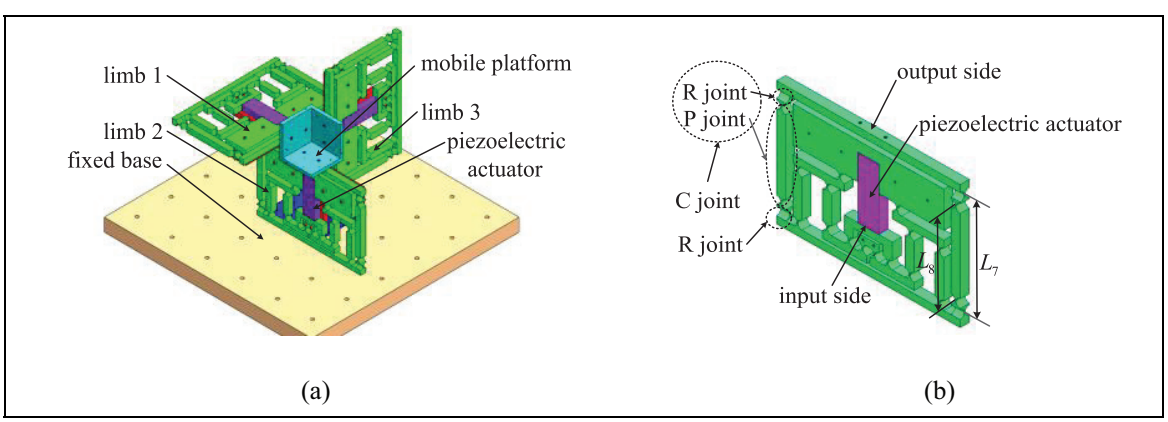

Figure 1. 3-PRC-compliant parallel micromanipulator: (a) the structure of micromanipulator and (b) the structure of limb.

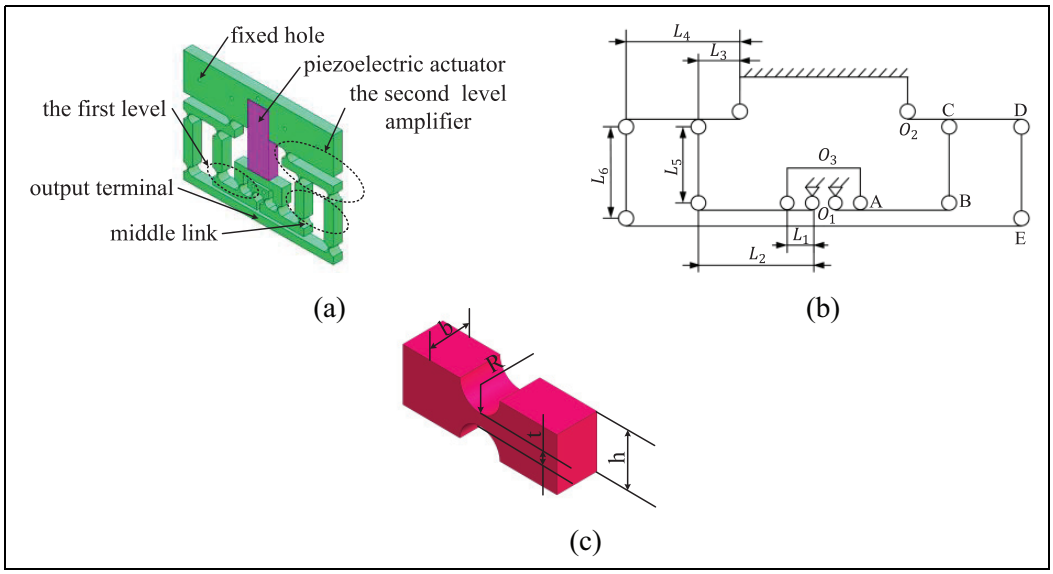

Figure 2. The secondary lever amplifier: (a) the novel secondary lever amplifier, (b) the geometric parameters of amplifier, and (c) the right circular flexure hinge.

Table 1. Geometric parameters of the secondary lever amplifier (unit: mm).

Parameters	Length	Parameters	Length	Parameters	Length
L_1	9.5	L_2	25	L_3	9
L_4	30	L_5	26	L_6	33
L_7	73.5	L_8	59.5	R	3
t	0.5	h	6.5	b	6.5

limbs with identical PRC structure, and the size of the entire 3-PRC parallel micromanipulator is 174.50 mm × 174.50 mm × 174.50 mm. The structure of each limb is depicted in Figure 1(b), and the secondary lever amplifier as a prismatic (P) hinge is fixed at the base and actuated by a PZT actuator. Cylindrical (C) joint is equivalent to revolute (R) joint and prismatic (P) hinge in axial direction, combined with revolute (R) joint as passive joints connected with mobile platform. In order to generate a cuboid shape workspace of the micromanipulator, each limb is designed as parallel mechanism to improve the rigidity and kinematics performance of the micromanipulator. Three limbs are assembled in the orthogonal design method to eliminate or reduce parasitic motions of the end-effector (mobile platform).

The secondary lever amplifier design

According to the lever principle, the novel secondary lever amplifier is designed to compensate the stroke of the piezoelectric actuator and then enlarge the mobile platform workspace. As illustrated in Figure 2(a), to reduce the overall size of the amplifier structure, the piezoelectric actuator was installed inside it. And the amplifier is designed as a symmetrical (parallel) structure for the purposes of eliminating the parasitic movement and improving the output accuracy of the amplifier. The novel amplifier fully owns both advantages of lever amplifier and bridge type amplifier which are with simple and compactness structure, good linearity.

As shown in Figure 2(b), O_1 point and O_2 point are the level pivots, O_3 point is the input side of PZT actuator, O_1AB is the first level and O_2CD is the second level, and the piezoelectric actuator exerts a small displacement at O_3. And then the output terminal E obtains ampliative displacement under the effect of O_1AB and O_2CD. As shown in Figure 2(c), all joints in the micromanipulator are expressed by the straight circular flexure hinge.

The geometric parameters are shown in Table 1, and the first lever and secondary lever theoretical amplification ratio A_1 and A_2 can be expressed as

$$A_1 = \frac{L_2}{L_1} = 2.632, \quad A_2 = \frac{L_2 L_4}{L_1 L_3} = 8.772 \qquad (1)$$

The theoretical output displacement of the secondary lever amplifier can be calculated by the following equation

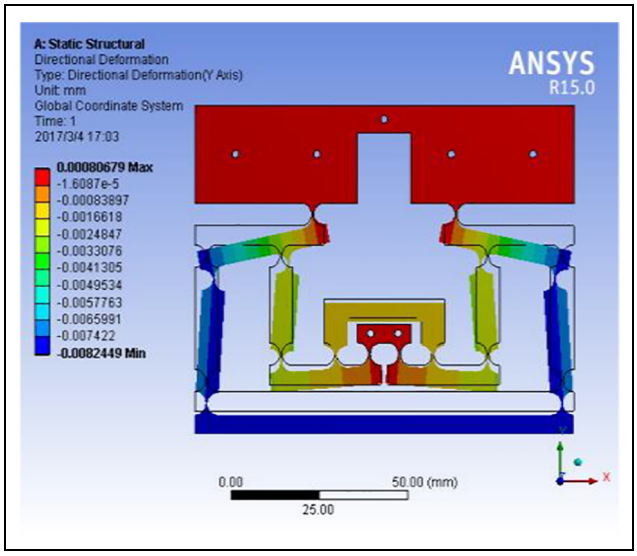

Figure 3. Deformation of the novel secondary lever amplifier.

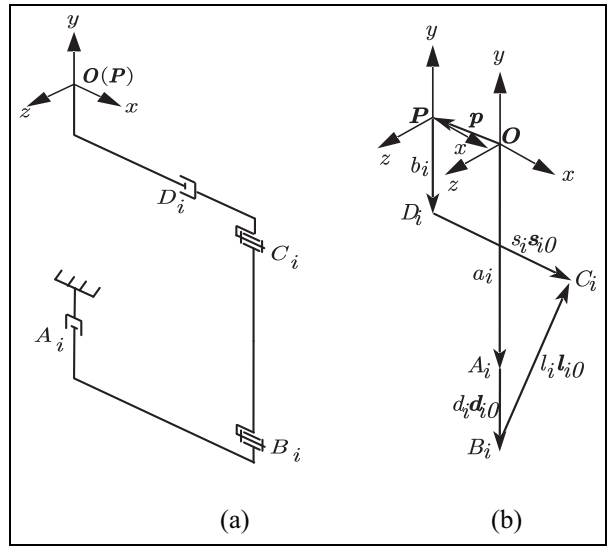

Figure 4. 3-PRC model of limb: (a) the simplified CAD model of limb and (b) schematic diagram of a 3-PRC limb.

$$d_i = A_2 q_i (i = 1, 2, 3) \tag{2}$$

The ANSYS software is used to verify the theoretical amplification ratio and the deformed shape is illustrated in Figure 3. The finite element analysis (FEA) results show that the amplification ratio A_{act}

$$A_{\text{act}} = \frac{y_{out}}{y_{in}} = 8.245 \tag{3}$$

Due to the elimination of the parasitic movement of the X axis, the theoretical amplification ratio A_2 of Y axis is different from the FEA result, but the result gives a very small percentage of error rate 6.01%.

Kinematics model of the 3-PRC-compliant parallel micromanipulator

The simplified computer-aided design (CAD) model of a 3-PRC-compliant parallel micromanipulator limb is graphically shown in Figure 4(a), and the schematic diagram is illustrated in Figure 4(b), each limb connects the fixed base to the mobile platform through a P joint, an R joint, and a C(R-P) joint in sequence, where the P joint is driven by PZT actuator mounted on the fixed base. The mobile platform is attached to the base by three identical PRC linkages. We assign a fixed Cartesian frame $\boldsymbol{O}\{x, y, z\}$ at the centered point P of the mobile platform, and the position of the mobile platform with respect to the reference frame can be described by a position vector on a moving frame $\boldsymbol{p} = [x\ y\ z]^{\mathrm{T}}$ of the reference point P.

With the vectors representation shown in Figure 4(b), the vectors can be expressed as

$$\left.\begin{aligned} \overrightarrow{OA_i} = \boldsymbol{a}_i, \overrightarrow{A_iB_i} = d_i\boldsymbol{d}_{io}, \overrightarrow{B_iC_i} = l_i\boldsymbol{l}_{io} \\ \overrightarrow{D_iC_i} = s_i\boldsymbol{s}_{io}, \overrightarrow{PD_i} = \boldsymbol{b}_i, i = 1, 2, 3 \end{aligned}\right\} \tag{4}$$

where $\boldsymbol{d}_{io}$, $\boldsymbol{l}_{io}$, and $\boldsymbol{s}_{io}$, respectively, indicate the unit vector along $\overrightarrow{A_iB_i}$, $\overrightarrow{B_iC_i}$, $\overrightarrow{D_iC_i}$; d_i and s_i are the moving distance of A_i joint and D_i joint, respectively. $|\boldsymbol{a}_i|$ is the distance from the fixed base to the A_i joint and $|\boldsymbol{b}_i|$ is the distance from the mobile platform to the D_i joint.

Inverse kinematics modeling mobility

As shown in Figure 4(b), a vector-loop equation can be written for ith limb of the 3-PRC model as follows

$$l_i\boldsymbol{l}_{io} = \boldsymbol{p} + \boldsymbol{R}_p b_i + s_i\boldsymbol{R}_p\boldsymbol{s}_{io} - \boldsymbol{a}_i - d_i\boldsymbol{d}_{io} \tag{5}$$

where $\boldsymbol{R}_p$ defines the rotation matrix from the reference frame $\boldsymbol{P}$ to fixed Cartesian frame $\boldsymbol{O}$ and is equaled to identity matrices. The square of both sides of formula (5) can be obtained

$$l_i^2 = \boldsymbol{D}_i^{\mathrm{T}}\boldsymbol{D}_i - 2d_i\boldsymbol{d}_{io}^{\mathrm{T}}\boldsymbol{D}_i + d_i^2 \tag{6}$$

with the notation of

$$\boldsymbol{D}_i = \boldsymbol{p} + \boldsymbol{R}_p\boldsymbol{b}_i + s_i\boldsymbol{R}_p\boldsymbol{s}_{io} - \boldsymbol{a}_i$$

In view of equation (5), a necessary calculation leads to the inverse displacement solutions

$$d_i = \boldsymbol{d}_{io}^{\mathrm{T}}\boldsymbol{D}_i \pm \sqrt{\left(\boldsymbol{d}_{io}^{\mathrm{T}}\boldsymbol{D}_i\right)^2 - \boldsymbol{D}_i^{\mathrm{T}}\boldsymbol{D}_i + l_i^2} \tag{7}$$

We can observe that there exist two solutions for variable, only the positive square root in equation (7) is selected

$$d_i = \boldsymbol{d}_{io}^{\mathrm{T}}\boldsymbol{D}_i + \sqrt{\left(\boldsymbol{d}_{io}^{\mathrm{T}}\boldsymbol{D}_i\right)^2 - \boldsymbol{D}_i^{\mathrm{T}}\boldsymbol{D}_i + l_i^2} \tag{8}$$

which can be expanded into the following forms

$$\left.\begin{aligned} d_1 &= -x - l + \sqrt{l^2 - y^2 - z^2} \\ d_2 &= -y - l + \sqrt{l^2 - x^2 - z^2} \\ d_3 &= -z - l + \sqrt{l^2 - x^2 - y^2} \end{aligned}\right\} \tag{9}$$

From equations (2) and (9), we can derive that

$$\boldsymbol{q} = \frac{1}{A_2}\begin{bmatrix} -x - l + \sqrt{l^2 - y^2 - z^2} \\ -y - l + \sqrt{l^2 - x^2 - z^2} \\ -z - l + \sqrt{l^2 - x^2 - y^2} \end{bmatrix} \tag{10}$$

which is inverse kinematics of the 3-PRC-compliant parallel micromanipulator.

Velocity analysis

Both sides of formula (5) are multiplied by s_i

$$0 = \boldsymbol{s}_{io}^{\mathrm{T}}\boldsymbol{p} + s_i\boldsymbol{s}_{io}^{\mathrm{T}}\boldsymbol{R}_p\boldsymbol{s}_{io} - \boldsymbol{s}_{io}^{\mathrm{T}}\boldsymbol{a}_i \tag{11}$$

And then it can be expanded into the following forms

$$\boldsymbol{s}_i = \left(\boldsymbol{s}_{io}^{\mathrm{T}}\boldsymbol{a}_i - \boldsymbol{s}_{io}^{\mathrm{T}}\boldsymbol{p}\right)/\boldsymbol{s}_{io}^{\mathrm{T}}\boldsymbol{R}_p\boldsymbol{s}_{io} \tag{12}$$

Following formula (12), differential equations with respect to time

$$\dot{s}_i = -\boldsymbol{s}_{io}^{\mathrm{T}}\dot{\boldsymbol{p}}/\boldsymbol{s}_{io}^{\mathrm{T}}\boldsymbol{R}_p\boldsymbol{s}_{io} \tag{13}$$

Formula (13) can be written as

$$\dot{\boldsymbol{s}} = \boldsymbol{J}_s\dot{\boldsymbol{p}} \tag{14}$$

where

$$\boldsymbol{J}_s = \begin{bmatrix} -\boldsymbol{s}_{1o}^{\mathrm{T}}\dot{\boldsymbol{p}}/\boldsymbol{s}_{1o}^{\mathrm{T}}\boldsymbol{R}_p\boldsymbol{s}_{1o} \\ -\boldsymbol{s}_{2o}^{\mathrm{T}}\dot{\boldsymbol{p}}/\boldsymbol{s}_{2o}^{\mathrm{T}}\boldsymbol{R}_p\boldsymbol{s}_{2o} \\ -\boldsymbol{s}_{3o}^{\mathrm{T}}\dot{\boldsymbol{p}}/\boldsymbol{s}_{3o}^{\mathrm{T}}\boldsymbol{R}_p\boldsymbol{s}_{3o} \end{bmatrix} \tag{15}$$

Substituting equation (6) into equation (5) and differentiating the expression with respect to time leads to

$$l_i\boldsymbol{\omega}_i\boldsymbol{l}_{io} = \dot{\boldsymbol{p}} + \dot{s}_i\boldsymbol{R}_p\boldsymbol{s}_{io} - \dot{d}_i\boldsymbol{d}_{io} \tag{16}$$

where $\boldsymbol{\omega}_i$ (i = 1,2,3) is the angular velocity of ith limb with B_i joint and C_i joint.

Dot-multiplying both sides of equation (16) by $\boldsymbol{l}_{io}$

$$\dot{\boldsymbol{d}}\boldsymbol{l}_{io}^{\mathrm{T}}\boldsymbol{d}_{io} = \boldsymbol{l}_{io}^{\mathrm{T}}\dot{\boldsymbol{p}} \tag{17}$$

Substituting equation (8) into equation (5), the unit vector expression for connecting the R joint B_i and the R joint C_i in the fixed coordinate system $\boldsymbol{O}$

$$\boldsymbol{l}_{io} = \frac{\left[\boldsymbol{D}_i - \left(\boldsymbol{d}_{io}^{\mathrm{T}}\boldsymbol{D}_i - \sqrt{\left(\boldsymbol{d}_{io}^{\mathrm{T}}\boldsymbol{D}_i\right)^2 - \boldsymbol{D}_i^{\mathrm{T}}\boldsymbol{D}_i + l_i^2}\right)\boldsymbol{d}_{io}\right]}{l_i} \tag{18}$$

Writing equation (17) three times, once for each i = 1, 2, and 3, yields three scalar equations which can be written in the matrix form

$$\boldsymbol{J}_d\dot{\boldsymbol{d}} = \boldsymbol{J}_p\dot{\boldsymbol{p}} \tag{19}$$

where the matrices

$$\dot{\boldsymbol{d}} = \begin{bmatrix}\dot{d}_1 & \dot{d}_2 & \dot{d}_3\end{bmatrix}^{\mathrm{T}},$$

$$\boldsymbol{J}_d = \begin{bmatrix} \boldsymbol{l}_{1o}^{\mathrm{T}}\boldsymbol{d}_{1o} & 0 & 0 \\ 0 & \boldsymbol{l}_{2o}^{\mathrm{T}}\boldsymbol{d}_{2o} & 0 \\ 0 & 0 & \boldsymbol{l}_{3o}^{\mathrm{T}}\boldsymbol{d}_{3o} \end{bmatrix}, \boldsymbol{J}_p = \begin{bmatrix}\boldsymbol{l}_{1o}^{\mathrm{T}} & \boldsymbol{l}_{2o}^{\mathrm{T}} & \boldsymbol{l}_{3o}^{\mathrm{T}}\end{bmatrix}^{\mathrm{T}}$$

the following velocity equations can be derived from equation (19)

$$\dot{\boldsymbol{d}} = \boldsymbol{J}\dot{\boldsymbol{p}} \tag{20}$$

where

$$\boldsymbol{J} = \boldsymbol{J}_d^{-1}\boldsymbol{J}_p = \begin{bmatrix} \dfrac{\boldsymbol{l}_{1o}}{\boldsymbol{l}_{1o}^{\mathrm{T}}\boldsymbol{d}_{1o}} & \dfrac{\boldsymbol{l}_{2o}}{\boldsymbol{l}_{2o}^{\mathrm{T}}\boldsymbol{d}_{2o}} & \dfrac{\boldsymbol{l}_{3o}}{\boldsymbol{l}_{3o}^{\mathrm{T}}\boldsymbol{d}_{3o}} \end{bmatrix}^{\mathrm{T}} \tag{21}$$

is the 3×3 Jacobian matrix of a 3-PRC-compliant parallel micromanipulator, and it plays an important role in kinematic analysis.

It can be expanded into the following form

$$\boldsymbol{J} = -\begin{bmatrix} 1 & \dfrac{y}{x + l - d_1} & \dfrac{z}{x + l - d_1} \\ \dfrac{x}{y + l - d_2} & 1 & \dfrac{z}{y + l - d_2} \\ \dfrac{x}{z + l - d_3} & \dfrac{y}{z + l - d_3} & 1 \end{bmatrix}$$

Forward kinematics modeling mobility

Considering the units for the actuated joint variable d_i and the mobile position x, y, z of the micromanipulator are micrometers, where the unit for l is millimeter, the Jacobian matrix can be approximately written as

$$\boldsymbol{J} \approx -\boldsymbol{I} \tag{22}$$

Equation (9) can be written as

$$\left.\begin{aligned} d_1 &\approx -x \\ d_2 &\approx -y \\ d_3 &\approx -z \end{aligned}\right\} \tag{23}$$

and then

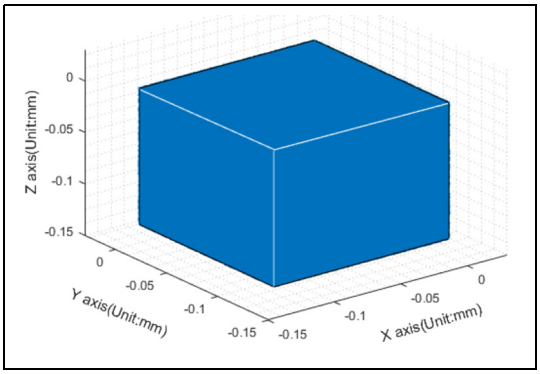

Figure 5. Reachable workspace of the micromanipulator.

$$\boldsymbol{d} = -\boldsymbol{Ip} \tag{24}$$

substituting equation (6) into equation (5)

$$\boldsymbol{q} = -\frac{1}{A_2}\boldsymbol{Ip} \tag{25}$$

So, the relationship between input stroke of piezoelectric actuators and the position of the central platform can be written as follows

$$\boldsymbol{p} = -A_2\boldsymbol{Iq} \tag{26}$$

Workspace analysis

The workspace of the 3-PRC-compliant parallel micromanipulator can be calculated by the aforementioned kinematic analysis. Actually, the reachable workspace of the manipulator not only depends on the above equation (10) but also has the relationship with material property. The following list is the constraint condition of 3-PRC-compliant parallel micromanipulator

$$\left.\begin{array}{c} 0 \le q_i \le q_{\max} = 15\ \mu\text{m}, i = 1,2,3 \\ l = L_7 = 73.5\ \text{mm} \end{array}\right\} \tag{27}$$

where q_i denotes the output displacement of the piezoelectric and l is the length of the R-C leg. Substituting equation (27) into equation (10), the workspace of the micromanipulator can be obtained by MATLAB, and the three-dimensional (3D) workspace is graphically illustrated in Figure 5. From the simulation results, the reachable workspace of the end-effector is a hexahedron.

Dynamics model of the 3-PRC-compliant parallel micromanipulator

Due to the merits of eliminating the consideration for the forces of constraint, Lagrange's equation of motion is adopted for the dynamics modeling of the 3-PRC-compliant parallel micromanipulator. In order to obtain the dynamics model, both the potential and kinetic energies of the micromanipulator should be expressed in terms of the selected coordinates and their derivatives, and the variable q is chosen as the generalized coordinates. And then assume that all of the potential energy come from the elastic deformations of flexure hinges and the gravity of the micromanipulator. The mass distribution of each component is shown in Figure 6.

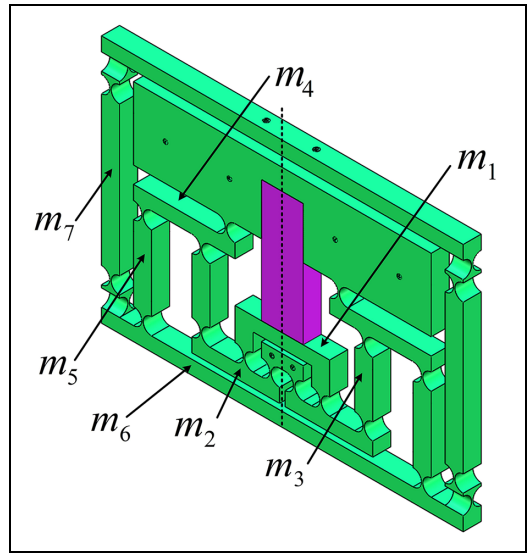

Figure 6. The mass distribution of components.

Potential and kinetic energy of the micromanipulator

The elastic potential energy for the second limb of secondary lever amplifier can be expressed as

$$\begin{aligned} U_2^{pa} &= 2\left(4 \times \frac{1}{2}k\theta_1^2 + 3 \times \frac{1}{2}k\theta_2^2\right) \\ &= \frac{4Ebt^{2.5}}{9\pi r^{0.5}}\left(\frac{2A_1^2q_2^2}{L_2^2} + \frac{3A_2^2q_2^2}{2L_4^2}\right) \end{aligned} \tag{28}$$

where k is the rotation stiffness of flexure R hinges, which can be expressed as

$$k = \frac{2Ebt^{2.5}}{9\pi r^{0.5}}$$

and the first lever angle θ_1 and secondary lever angle θ_2 can be expressed as

$$\theta_1 = \frac{A_1q_i}{L_2},\ \theta_2 = \frac{A_2q_i}{L_4}$$

the kinetic energy of the secondary lever amplifier can be calculated by the following equation

$$T_2^{pa} = 2\left[\frac{1}{2}m_1\dot{q}_2^2 + \frac{1}{2}I_{G2}\dot{\theta}_1^2 + \frac{1}{2}m_3(A_1\dot{q}_2)^2 + \frac{1}{2}I_{G3}\dot{\theta}_1^2 + \frac{1}{2}I_{G4}\dot{\theta}_2^2 + \frac{1}{2}(m_5+m_6)(A_2\dot{q}_2)^2 + \frac{1}{2}I_{G5}\dot{\theta}_2^2\right]$$
$$= \left[m_1 + \frac{1}{3}m_2 + \left(1 + \frac{L_5^2}{12L_2^2}\right)m_3\right]A_1^2\dot{q}_2^2 + \left[\frac{1}{3}m_4 + \left(1 + \frac{L_6^2}{12L_4^2}\right)m_5 + m_6\right]A_2^2\dot{q}_2^2 \quad (29)$$

where rotary inertia of the components can be expressed by

$$I_{G2} = \frac{1}{3}m_2L_2^2,\ I_{G3} = \frac{1}{12}m_3L_5^2,\ I_{G4} = \frac{1}{3}m_4L_4^2,\ I_{G5} = \frac{1}{3}m_5L_6^2$$

thus, the energy function for the three limbs secondary lever amplifier of the micromanipulator can be computed by

$$L_{Pa} = \sum_{i=1}^{3}\left(T_i^{Pa} - U_i^{Pa}\right) \quad (30)$$

The potential energy for the second R-C leg of micromanipulator can be obtained by

$$U_2^{Leg} = 4\times\frac{1}{2}k\left(\beta_2^2 + \gamma_2^2\right) = \frac{4Ebt^{2.5}A^2}{9\pi r^{0.5}}\left(\frac{q_3^2}{L_7^2} + \frac{q_1^2}{L_8^2}\right) \quad (31)$$

where

$$\beta_2 = \frac{z}{L_8},\ \gamma_2 = \frac{x}{L_7}$$

The kinetic energy of the second R-C leg can be expressed as

$$T_2^{Leg} = 2\left\{\frac{1}{2}m_7\left[(A_2\dot{q}_2)^2 + \left(\frac{\dot{z}}{2}\right)^2 + \left(\frac{\dot{x}}{2}\right)^2\right] + \frac{1}{2}\left(I_{G6}\dot{\beta}_2^2 + I_{G7}\dot{\gamma}_2^2\right)\right\} = \frac{5}{3}A_2^2m_7\dot{q}_2^2 \quad (32)$$

where rotary inertia of the components can be expressed by

$$I_{G6} = \frac{1}{12}m_7L_8^2,\ I_{G7} = \frac{1}{12}m_7L_7^2$$

thus, the energy function for the three limbs R-C leg of the micromanipulator can be computed by

$$L_{Leg} = \sum_{i=1}^{3}\left(T_i^{Leg} - U_i^{Leg}\right) \quad (33)$$

The kinetic energy for the mobile platform is expressed by

$$T_{Mp} = \frac{1}{2}m_0\left(\dot{x}^2 + \dot{y}^2 + \dot{z}^2\right) = \frac{1}{2}m_0A_2^2\left(\dot{q}_1^2 + \dot{q}_2^2 + \dot{q}_3^2\right) \quad (34)$$

The potential energy of the entire micromanipulator due to the gravitational force should be considered

$$U_G = [m_0A_2 + 6(m_1+m_2+m_3)A_1 + 6(m_4+m_5+m_6+m_7)A_2]gq_2 \quad (35)$$

Lagrange's function for the micromanipulator can be generated

$$L = L_{Pa} + L_{Leg} + T_{Mp} - U_G \quad (36)$$

Lagrange's equation of motion can be derived based on the generalized coordinates q, according to

$$\frac{d}{dt}\cdot\frac{\partial L}{\partial \dot{q}_i} - \frac{\partial L}{\partial q_i} = F_i \quad (37)$$

where q_i denotes the ith generalized coordinate and F_i is the ith actuation force.

The generated dynamic equations take on the following form

$$\boldsymbol{M}\ddot{\boldsymbol{q}} + \boldsymbol{K}\boldsymbol{q} + \boldsymbol{G} = \boldsymbol{F} \quad (38)$$

where $\boldsymbol{M} = diag\{M_e\}$ is the mass matrix, $\boldsymbol{K} = diag\{K_e\}$ is the stiffness, $\boldsymbol{G} = [0 \quad G_e \quad 0]^{\mathrm{T}}$ is the gravity force vector, and $\boldsymbol{F} = [F_1 \quad F_2 \quad F_3]^{\mathrm{T}}$ is the actuation force. Respectively, with the following notations

$$M_e = 2\left[m_1 + \frac{m_2}{3} + \left(1 + \frac{L_5^2}{12L_2^2}\right)m_3\right]A_1^2 + \left[\frac{2}{3}m_4 + 2\left(1 + \frac{L_6^2}{12L_4^2}\right)m_5 + 2m_6 + \frac{10}{3}m_7 + m_0\right]A_2^2$$
$$K_e = \frac{8Ebt^{2.5}}{9\pi r^{0.5}}\left[\frac{2A_1^2}{L_2^2} + \frac{3A_2^2}{2L_4^2} + \left(\frac{1}{L_7^2} + \frac{1}{L_8^2}\right)\right]$$
$$G_e = [m_0A_2 + 6(m_1+m_2+m_3)A_1 + 6(m_4+m_5+m_6+m_7)A_2]g$$

where m_0 is the mass of the mobile platform.

Modal analysis of the micromanipulator

The modal analysis is necessary for the design of 3-PRC-compliant parallel micromanipulator as far as the control frequency is concerned, and the dynamic

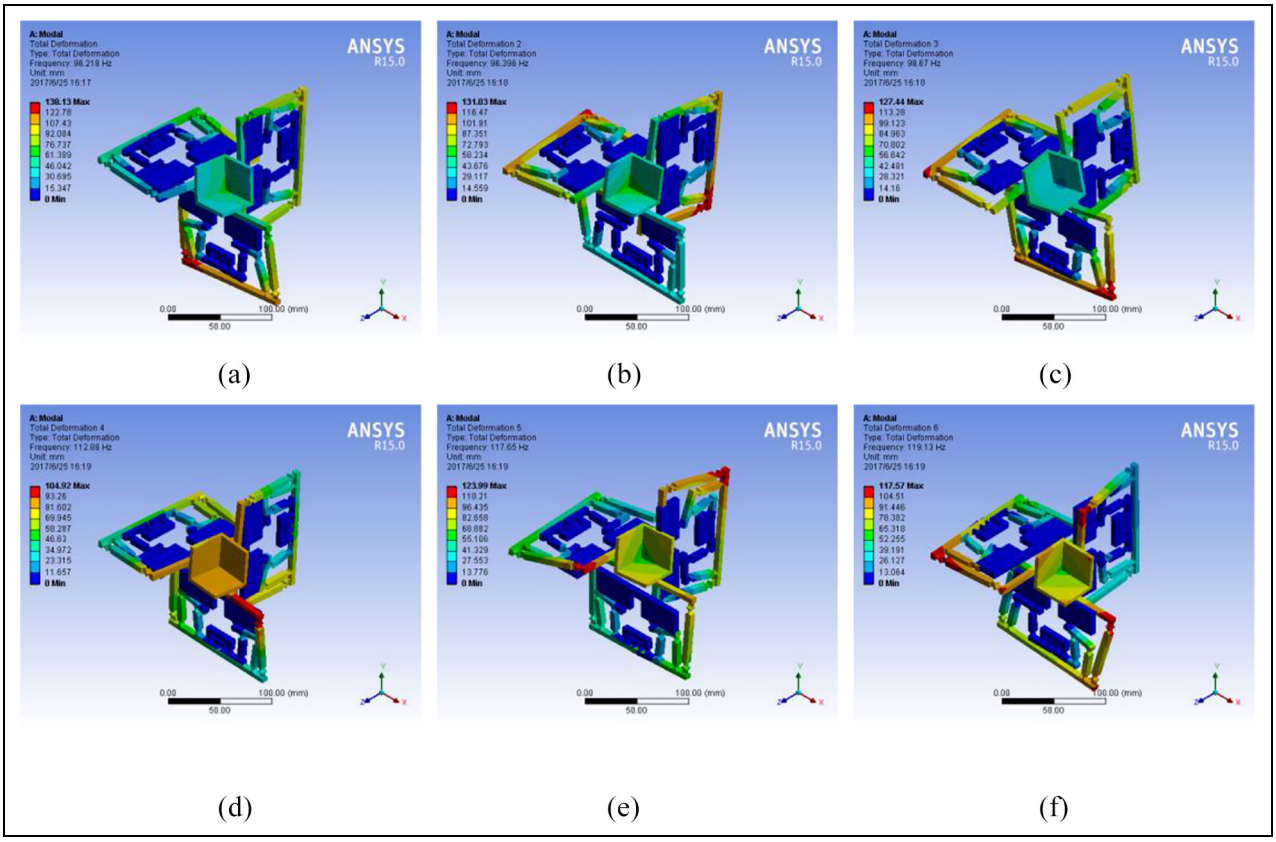

Figure 7. The first six modal shapes: (a) modal shape 1, (b) modal shape 2, (c) modal shape 3, (d) modal shape 4, (e) modal shape 5, and (f) modal shape 6.

equation of undamped free vibration of the micromanipulator system can be expressed as

$$\boldsymbol{M}\ddot{\boldsymbol{q}} + \boldsymbol{K}\boldsymbol{q} = 0 \tag{39}$$

The condition of non-zero solutions for equation (39) can be derived by

$$|\boldsymbol{K} - \lambda_i \boldsymbol{M}| = 0 \tag{40}$$

where $\lambda_i = \omega_i^2$, $f_i = \omega_i/2\pi$.

The natural frequency of the micromanipulator can be calculated by

$$f = \frac{1}{2\pi}\sqrt{\frac{K_e}{M_e}} = 93.83\ \text{Hz} \tag{41}$$

The micromanipulator material adopts Al(7075-T6), the density is 2810 kg/m^3, Young's modulus E is 71.7 GPa, and Poisson's ratio is 0.33. The first six modal shapes are illustrated in Figure 7, and the first six natural frequencies of modal analysis are listed in Table 2. It is observed that the first natural frequency obtained by ANSYS software agrees well with the value calculated from equation (41). The deviation between the calculated and the simulated nature frequency is only 2.54%, which verifies the validity of the performance dynamic modeling for the 3-PRC-compliant parallel micromanipulator.

Table 2. The first six natural frequencies.

No.	Natural frequencies (Hz)	No.	Natural frequencies (Hz)
1	96.218	2	96.396
3	98.67	4	112.88
5	117.65	6	119.13

Conclusion

A compliant parallel micromanipulator based on translational 3-PRC parallel mechanism that can realize three translational DOFs in space is designed and analyzed in this article. The mechanism employs secondary lever amplifier to compensate the stroke of the piezoelectric actuator, and the deviation between the calculated and the simulated amplification ratio of the amplifier is only 6.01%. The inverse and forward kinematics and Jacobian matrix have been derived, and the reachable workspace is generated by simulation

analysis. The dynamics analysis of 3-PRC micromanipulator is also performed in this article, and Lagrange's equation of motion is adopted for the dynamics modeling of the micromanipulator. The natural frequency is calculated, which is verified by the modal analysis via Workbench software, and the deviation between the calculated and the simulated nature frequency is only 2.54%. The results show that this micromanipulator has a favorable performance on kinematics and dynamics, and this micromanipulator can achieve micro/nano level motion with high accuracy. To further validate the performance of proposed mechanism, the experimental studies will be conducted in next stage, including prototype fabrication and workspace validation.

Declaration of conflicting interests

The author(s) declared no potential conflicts of interest with respect to the research, authorship, and/or publication of this article.

Funding

The author(s) disclosed receipt of the following financial support for the research, authorship, and/or publication of this article: This paper was co-supported by National Natural Science Foundation of China (Grant No. 51575544) and Tianjin Natural Science Foundation Key Program (Grant No. 16JCZDJC38000).

ORCID iD

Xiang-Chun Li https://orcid.org/0000-0003-0031-2357

References

1. Li C, Gu G, Yang M, et al. Design, analysis and testing of a parallel-kinematic high-bandwidth XY nanopositioning stage. *Rev Sci Instrum* 2013; 84: 1–12.
2. Kim J-J, Choi Y-M, Ahn D, et al. A millimeter-range flexure-based nano-positioning stage using a self-guided displacement amplification mechanism. *Mech Mach Theory* 2012; 50: 109–120.
3. Deshmukh B and Pardeshi S. Study of various compliant micromechanism and introduction of a compliant micromotion replicating mechanism. *Int J Mech Eng Technol* 2012; 3: 574–582.
4. Ouyang PR, Zhang WJ, Gupta MM, et al. Overview of the development of a visual based automated biomicromanipulation system. *Mechatronics* 2007; 17: 578–588.
5. Reza Moheimani SO. Invited review article: accurate and fast nanopositioning with piezoelectric tube scanners: emerging trends and future challenges. *Rev Sci Instrum* 2008; 79: 1–11.
6. Lu Z, Moraes C, Zhao Y, et al. A micromanipulation system for single cell deposition. In: *Proceedings of the IEEE International Conference on Robotics and Automation*, Anchorage, AK, 3–7 May 2010, pp.494–499. New York: IEEE.
7. Ding B, Yang ZX, Zhang G, et al. Optimum design and analysis of flexure based mechanism for non-circular diamond turning operation. *Adv Mech Eng* 2017; 9: 1–10.
8. Zhang LS, Liu YB, Huang L, et al. Using output voltage of charge drivers to reduce hysteresis of piezoelectric actuators. *Electron Lett* 2012; 48: 697–698.
9. Jalili N, Wagner J and Dadfarnia M. A piezoelectric driven ratchet actuator mechanism with application to automotive engine valves. *Mechatronics* 2003; 13: 933–956.
10. Tian Y, Shirinzadeh B, Zhang D, et al. Design and forward kinematics of the compliant micro-manipulator with lever mechanisms. *Precis Eng* 2009; 33: 466–475.
11. Li Y and Xu Q. Development and assessment of a novel decoupled XY parallel micropositioning platform. *IEEE T Mech* 2010; 15: 125–135.
12. Kao C-C and Fung R-F. Using the modified PSO method to identify a Scott-Russell mechanism actuated by a piezoelectric element. *Mech Syst Signal Pr* 2009; 23: 1652–1661.
13. Ding B, Li Y, Xiao X, et al. Design and analysis of a 3-DOF planar micromanipulation stage with large rotational displacement for micromanipulation system. *Mech Sci* 2017; 8: 117–126.
14. Liu P, Yan P and Zhang Z. Design and analysis of an X-Y parallel nanopositioner supporting large-stroke servomechanism. *Proc IMechE, Part C: J Mechanical Engineering Science* 2014; 229: 364–376.
15. Li Y and Xu Q. A novel piezoactuated XY stage with parallel, decoupled, and stacked flexure structure for micro-/nanopositioning. *IEEE T Ind Electron* 2011; 58: 3601–3615.
16. Li Y and Xu Q. Design and analysis of a totally decoupled flexure-based XY parallel micromanipulator. *IEEE T Robot* 2009; 25: 645–657.
17. Muraoka M and Sanada S. Displacement amplifier for piezoelectric actuator based on honeycomb mechanism. *Sensor Actuat A: Phys* 2010; 157: 84–90.
18. Yong YK, Aphale SS and Reza Moheimani SO. Design, identification, and control of a flexure-based XY stage for fast nanoscale positioning. *IEEE T Nanotechnol* 2009; 8: 46–54.
19. Bhagat U, Shirinzadeh B, Clark L, et al. Design and analysis of a novel flexure-based 3-DOF mechanism. *Mech Mach Theory* 2014; 74: 173–187.
20. Li Y and Xu Q. A totally decoupled piezo-driven XYZ flexure parallel micropositioning stage for micro/nanomanipulation. *IEEE T Autom Sci Eng* 2011; 8: 265–279.
21. Li Y and Xu Q. Design and optimization of an XYZ parallel micromanipulator with flexure hinges. *J Intell Robot Syst* 2009; 55: 377–402.